PAPER

Check for updates

Trajectory surface hopping molecular dynamics simulations for retinal protonated Schiff-base photoisomerization†

Yuxiu Liu[a] and Chaoyuan Zhu ⓘ ★[ab]

Global switching trajectory surface hopping molecular dynamics simulations are performed using accurate on-the-fly (TD)CAM-B3LYP/6-31G potential energy surfaces to study retinal protonated Schiff-base photoisomerization up to S_1 excitation. The simulations detected two-layer conical intersection networks: one is at an energy as high as 8 eV and the other is in the energy range around 3–4 eV. Six conical intersections within the low-layer energy region that correspond to active conical intersections under experimental conditions are found *via* the use of pairwise isomers, within which nonadiabatic molecular dynamics simulations are performed. Eight isomer products are populated with simulated sampling trajectories from which the simulated quantum yield in the gas phase is estimated to be 0.11 (0.08) moving from the all-*trans* isomer to the 11-*cis* (11-*cis* to all-*trans*) isomer in comparison with an experimental value of 0.09 (0.2) in the solution phase. Each conical intersection is related to one specific twist angle accompanying a related C=C double bond motion during photoisomerization. Nonplanar distortion of the entire dynamic process has a significant role in the formation of the relevant photoisomerization products. The present simulation indicates that all hopping points show well-behaved potential energy surface topology, as calculated *via* the conventional TDDFT method, at conical intersections between S_1 and S_0 states. Therefore, the present nonadiabatic dynamics simulations with the TDDFT method are very encouraging for simulating various large systems related to retinal Schiff-base photoisomerization in the real world.

1. Introduction

The retinal protonated Schiff-base (RPSB) in its all-*trans* form is found in bacterial rhodopsin, and it is isomerized upon photoexcitation from its native all-*trans* form to the 13-*cis* form with an ultrafast speed of 500 fs and a quantum yield of about 0.6–0.7.[1–3] In contrast, the analogous photoisomerization process in solution is slow with a speed of about 4 ps and a poor total quantum yield of about 0.1–0.3;[2,4,5] it also involves the formation of the isomerized products: the 9-*cis* form with a quantum yield of 0.02, the 11-*cis* form with a quantum yield of 0.09, and the 13-*cis* form with a quantum yield of 0.04. In addition, the 11-*cis* RPSB chromophore is found in the retinal protein rhodopsin, exhibiting almost barrierless dynamics on the first excited state (S_1) potential energy surface (PES),[6,7] and the 11-*cis* form is isomerized to the all-*trans* form

within as little as 200 fs, and the quantum yield is 0.65 *via* a low-lying S_1/S_0 conical intersection (CI).[8–10] However, in methanol solution, 11-*cis* RPSB isomerization also takes as long as 4 ps.[11–13] Current experimental measurements and theoretical estimations show that the RPSB in protein environments can be isomerized with an ultrafast speed and high quantum yields and, especially for 11-*cis* RPSB, the protein frame can adjust the ground-state chromophore conformation, resulting in more reactive decay channels.[14] It is realized that the surrounding environment of the RPSB can have a significant influence on the photoisomerization processes related to the intrinsic retinal properties. Experimental studies in the gas phase of RPSB isomerization mainly focused on the absorption spectrum[15] and action spectroscopy;[16,17] in the cases of all-*trans* and 11-*cis* RPSB, experiments show that the energy gaps between the S_1 and S_0 states are about 420–680 nm,[16] and the lifetimes of electronically excited states manifest that the decay times are temperature dependent.[17] There is a fast decay component with a lifetime of about 650 ± 160 fs geared toward 11-*cis* RPSB and a slow component with a lifetime of around 4.7 ± 3 ps aimed toward all-*trans* RPSB. Therefore, all-*trans* RPSB is inclined to isomerize into the 11-*cis* form, while the fast

[a] *Department of Applied Chemistry and Institute of Molecular Science, National Chiao-Tung University, Hsinchu 30010, Taiwan. E-mail: cyzhu@mail.nctu.edu.tw*

[b] *Department of Applied Chemistry and Center for Emergent Functional Matter Science, National Yang Ming Chiao Tung University, Hsinchu 30010, Taiwan*

† Electronic supplementary information (ESI) available. See DOI: 10.1039/d1cp03401d

This journal is © the Owner Societies 2021

Phys. Chem. Chem. Phys., 2021, **23**, 23861–23874 | **23861**

photoresponse of the retinal chromophore is straightforwardly related to intrinsic retinal properties.[17]

Theoretical studies have been carried out for calculating the Franck–Condon excitation energies, equilibrium geometries, and photoisomerization reaction pathways in relation to conical intersection (CI) in the gas phase.[17–24] Meanwhile, photoisomerization processes that take place on the potential energy surface are mostly related to the ground state S_0 and the first excited-state S_1, due to the fact that the energy gap between S_1 and S_2 is very large for RPSB chromophores in the gas phase.[18,20] Density functional theory (DFT) can easily be employed to optimize the equilibrium structures in the ground state, while time-dependent (TD)-DFT is utilized for calculating vertical excitation energies. Complete-active-space self-consistent-field (CASSCF) multireference, spin–flip (SF)-DFT, and SF-TD-DFT methods are usually employed to calculate the geometries of CI points and to scan related photoisomerization reaction pathways. High-level theoretical methods, such as CASPT2, NEVPT2, CR-EOM-CCSD(T), and EOM-CCSD, are employed to correct single-point energies *via* including dynamic electronic correlation for related geometry structures.[19,21] *Via* employing these high-level calculations, Kiefer and coworkers[17] reported small (30 cm^{-1}) and big ($\sim$300 cm^{-1}) potential barriers during internal conversion processes, starting from the Franck–Condon regions in the S_1 state, from the 11-*cis* and all-*trans* forms, respectively, consistent with similar high-level calculations performed by Aguilar and coworkers.[22] Actually, experiments and calculations have shown isomerization from the all-*trans* form to the 9-*cis*, 11-*cis*, and 13-*cis* forms, in which the cis isomers of RPSB have almost-barrierless fast 400 fs decay and the all-*trans* isomer exhibits barrier-controlled slow 3 ps decay.[17] Park and Shiozaki[23] performed XMS-CASPT2 calculations along the minimum CI energy path (MECI), and they found that the potential barrier from all-*trans* to 11-*cis* is lower than from all-*trans* to 13-*cis*. Regarding isomerization starting from 11-*cis* RPSB, however, most studies accepted the viewpoint of a nearly barrierless process on the S_1 PES with a sub-picosecond excited-state lifetime.[24–26] In contrast, Han and coworkers[19] performed SF-DTDFT calculations along the constructed linearly interpolated internal coordinate (LIIC) pathway of MECI and they found that there is a higher potential barrier of about 10 kcal mol^{-1} starting from the 11-*cis* form. This large potential energy barrier is not realistic, and large error might arise from spin contamination in the SF-TDDFT method.

Nonadiabatic *ab initio* dynamics simulation can be performed only using a simplified RPSB model.[24,27–31] In this way, Buss and coworkers[28] performed trajectory surface hopping dynamics simulations with the TDDFT method, and they found that chromophore distortion severely impacted the results of the photoreaction; in comparison with the reaction rate of the relaxed chromophore, the torsional characteristic dihedral angle increased the rate to some extent. Barbatti and coworkers[29] performed trajectory surface hopping dynamics simulations with the CASSCF method, and they found that the bond length alternation, defined as the difference between the averages of single bond and double bond lengths, was obviously altered in

the process of excitation, as was the twisted special dihedral angle; this is a significant finding due to the conical intersection within the photoisomerization dynamics. These model studies have claimed that lower photoproduct specificity during 11-*cis* and all-*trans* isomerization processes in the gas phase was obtained because isomerization is an intrinsic property of retinal chromophores. Meanwhile, due to the truncated model used, the acquired lower average excited-state lifetime of about 100 fs is inconsistent with experimental results.[17]

In the present work, we performed global trajectory surface hopping dynamic simulations with conventional TDDFT on-the-fly potential energy surfaces based on a real system (not a model system) of RPSB photoisomerization, including eight different isomers (all-*trans*, 7_8-*cis*, 8_11-*cis*, 9_11-*cis*, 11-*cis*, 11_14-*cis*, 9-*cis*, and 8-*cis* forms). We have demonstrated that a method based on a global switching algorithm (without calculating nonadiabatic vectors) plus TDDFT could be successfully applied to ultrafast photoisomerization dynamics simulations of a large dMe-OMe-NAIP system.[32] We first identify each conical intersection mainly related to one torsional dihedral angle that connects two photoproducts, and we then construct a conical intersection network, based on which real-system RPSB photoisomerization can be interpreted and analyzed.

2. Computational methods and detailed analysis

A global switching algorithm[33] (with simple and accurate Zhu-Nakamura analytical formulas[34,35]) is employed in cooperation with trajectory surface hopping molecular dynamics simulations associated with TDDFT using on-the-fly potential energy surfaces for real-system RPSB photoisomerization. Potential energy surfaces and their gradients are computed *via* employing the Gaussian 16 computational package.[36] The long-range corrected CAM-B3LYP hybrid functional is an encouraging method to calculate the excited states with a charge-transfer component[37] presented by retinal chromophores, and the 6-31G basis set of moderate size is employed.

The (TD)CAM-B3LYP/6-31G method (with charge of +1 and multiplicity of 1 for RPSB isomers) was employed for both optimizing the electronic structures of ground and first excited states and performing on-the-fly trajectory surface dynamics simulations. Vibrational frequency calculations are carried out to characterize the minima and saddle points with zero imaginary vibrational frequencies and one imaginary vibrational frequency, respectively. However, the conical intersection zones are found *via* running a few tens of sampling trajectories using the global-switching trajectory surface hopping method, and in each CI zone, one CI that has a minimum energy gap is identified as a representative conical intersection (the definition of CI used in this section is used throughout the present work).

Under the Born–Oppenheimer approximation, electronic motion is much faster than nuclear motion in molecules and, thus, a molecule with equilibrium geometry that absorbs light energy in the electronic ground state will be vertically excited to

an electronic excited state instantaneously. This means that nuclear motion is frozen when the molecule is excited from the ground state to the excited state, and this phenomenon is called the Franck–Condon principle. Theoretically speaking, we prepare initial conditions for the coordinates and velocities of sampling trajectories at the ground-state S_0 minimum (this region is called the Franck–Condon region), and then we vertically move these initial conditions to the excited S_1 state where the sampling trajectories start running. In order to localize the conical intersections, we preliminarily performed 20 sampling trajectories *via* dynamic simulations for up to 4000 fs starting from the all-*trans* Franck–Condon regions in the S_1 state with a total initial kinetic energy as high as 14 eV (above the all-*trans* energy as the energy zero point). All those sampling trajectories increase the potential energy in the S_1 state rapidly within a few femtoseconds, and then they oscillate around a potential energy of 8 eV in the S_1 state. None of them are able to make hops during the 4000 fs simulation time, and the minimum energy separation is kept much larger than 0.5 eV along all sampling trajectories. Fig. S1 (ESI†) shows that one such resonance trajectory keeps an oscillating structure starting from the all-*trans* form. Although the total initial kinetic energy of 14 eV is much higher than the potential energy barrier around the Franck–Condon regions in the all-*trans* form for all sampling trajectories, they still cannot overcome this potential energy barrier to run *via* conical intersection zones, and we believe that the effective kinetic energy projected from the total kinetic energy in a particular vibration mode is still not high enough to reach a transition state along the trajectory evolution pathway. This is because the total kinetic energy quickly dissipates into all vibrational modes during trajectory evolution. On the other hand, we also performed 20 sampling trajectories *via* dynamic simulations for up to 1000 fs starting from the 11-*cis* Franck–Condon regions in the S_1 state with a total initial kinetic energy of around 14 eV and we found 6 sampling trajectories making hops at around 8 eV. Fig. S2 (ESI†) shows that one such hopping trajectory makes a hop at 900 fs upon initially starting from the 11-*cis* form. This confirms that the potential energy barrier in the S_1 state is lower in the 11-*cis* form than in the all-*trans* form. The sampling trajectories starting from all-*trans* and 11-*cis* forms could only detect CI zones around 8 eV that do not correspond to situations seen under experimental conditions. We realized that CI zones might be classified into a high-layer-energy zone at around 8 eV and a low-layer-energy zone at around 3.5 eV. However, the sampling trajectories starting from the Franck–Condon regions of the all-*trans* and 11-*cis* forms do not lead to finding the CI in the low-layer-energy zone. We will figure out a new sampling scheme in the following discussion.

We found eight isomers in the ground state *via* optimization, and these are the all-*trans*, 7_8-*cis*, 8_11-*cis*, 9_11-*cis*, 11-*cis*, 11_14-*cis*, 9-*cis*, and 8-*cis* forms, as shown in Table 1 (the corresponding Cartesian coordinates are given in Table S1 (ESI†)). For each ground-state structure, we optimized the corresponding first-excited-state geometry (expect for the 7_8-*cis* form), as shown in Table 1, with blue colored text relating to

the geometries of the dihedral angles of excited states. Fig. 1 shows that seven dihedral angles (five of them, α, β, γ, δ, and ε, are listed in Table 1) are the most important ones relating to specific conical intersections. The global minimum is in the all-*trans* ground state, which is considered to be the energy zero point. In general, the single-*cis* isomers are lower in energy than the double-*cis* isomers; the S_0 potential energy values are 0.21 eV, 0.08 eV, and 0.11 eV for the 11-*cis*, 9-*cis*, and 8-*cis* isomers, respectively, in comparison with values of 0.28 eV, 0.24 eV, and 0.41 eV for the 8_11-*cis*, 9_11-*cis*, and 11_14-*cis* isomers, respectively. This conclusion is consistent with results discussed by Bieske and coworkers,[38] and it simply indicates that a cisoid conformation results in more steric hindrance effects on the molecular skeleton, especially along polyene conjugated chains, thus increasing the energy systematically. Vertical excitation energies in the S_0 state for all isomers calculated *via* the present CAM-B3LYP/6-31G method agree well with previous M06-2X/cc-pVDZ benchmark calculations,[38] as shown in Table 2. Actually, we made calculations using the TD-B3LYP method (not given in Table 2) as well, and we found that the results from TD-CAM-B3LYP are better than those from TD-B3LYP. On the contrary, vertical excitation energy calculations showed that TD-B3LYP is better than TD-CAM-B3LYP in comparison with the experimental results for a dMe-OMe-NAIP system.[32] The vertical excitation energies for all isomers are below 3 eV in the visible light range with significant oscillator strengths in the Franck–Condon regions, as shown in Table 1. For the 11-*cis* isomer, the vertical excitation energy in the present calculations in the gas phase is 2.79 eV in comparison with a maximum absorption of 2.81 eV observed in methanol solution[2,39] and 2.49 eV observed in rhodopsin.[40] For the all-*trans* isomer, the vertical excitation energy in the present calculations in the gas phase is 2.57 eV in comparison with a maximum absorption of 2.79 eV observed in methanol solution[2,39] and 2.18 eV observed in bacteriorhodopsin.[41] The vertical and adiabatic excitation energies in the S_1 state for each isomer are very close to each other, and this implies that the optimized S_0 and S_1 electronic structures for each isomer are very similar to each other in terms of the five important dihedral angles, as shown in Table 1. The calculated results are consistent with results simulated *via* quantum Monte Carlo (QMC), coupled cluster (CC), and CASPT2 methods where the bond-length pattern of the S_0 state is preserved in the S_1 state based on a truncated RPSB model.[42–46]

In order to localize each conical intersection that might connect two or three photoproducts of RPSB isomers, we first attempted to find transition states that connect two RPSB isomers. The 11-*cis*, 9-*cis*, and 8-*cis* isomers are the main photoisomerization products from the all-*trans* isomer because of the lower energies calculated in the gas phase along the minimum energy CI (MECI).[22,23,48] Meanwhile, the double-*cis* isomers, including 7_8-*cis*, 8_11-*cis*, 9_11-*cis*, and 11_14-*cis*, are also important in terms of the photoisomerization products as well.[38] We searched each CI zone between every pair of isomers among the 8 isomers, and we neglected all CI zones that have energy as high as 8 eV. This analysis led us to find seven CI

This journal is © the Owner Societies 2021

Phys. Chem. Chem. Phys., 2021, **23**, 23861–23874 | **23863**

Table 1 Key geometries for eight equilibrium isomers, three transition states (TS), and four rotation states (RS) in the ground state S_0, for seven equilibrium isomers in the excited state S_1, and for seven representative conical intersections (CIs). AT stands for the all-*trans* form, S_1(VE) stands for the vertical excitation energy in eV, and S_1(MIN) stands for the adiabatic excitation energy in eV. Five important dihedral angles, α, β, γ, δ, and ε, are defined in Fig. 1 (the numbers in parentheses are the oscillator strengths for isomers and the blue colored values show the adiabatic S_1 state geometries)

Structure	Potential energy			Dihedral angle				
	S_0	S_1(VE)	S_1(MIN)	α	β	γ	δ	ε
All-*trans*	0.00	2.57 (1.60)	2.48 (1.69)	−179.90	0.05	−180.00	179.99	−177.90
				179.75	0.01	179.36	179.85	−176.11
RS(AT/7_8-*cis*)	5.09	5.40		−179.84	0.17	−179.13	179.73	−100.92
7_8-*cis*	0.25	2.82 (0.92)		−179.78	0.30	−178.15	179.43	−13.42
CI(AT/7_8-*cis*)	5.26	5.34		−179.54	−0.05	−179.53	179.38	−100.61
TS(AT/11-*cis*)	0.78	2.78		−133.77	47.24	176.69	−176.25	175.64
CI(AT/11-*cis*)	2.94	3.13		−99.18	98.12	170.36	−170.65	−172.79
CI(AT/8_11-*cis*)	3.92	3.94		−88.74	87.70	177.52	179.77	−98.62
RS(AT/8_11-*cis*)	3.42	3.84		−88.55	91.66	177.83	179.95	−98.18
CI(AT/9_11-*cis*)	3.48	3.63		−80.25	85.64	−11.42	172.31	168.44
RS(AT/9_11-*cis*)	1.81	3.83		−54.04	125.93	−53.92	179.96	−177.68
8_11-*cis*	0.28	2.81 (1.37)	2.69 (1.41)	−0.78	179.67	175.74	179.92	−21.59
				−8.27	173.81	177.67	176.02	−9.95
9_11-*cis*	0.24	2.78 (1.54)	2.70 (1.35)	−0.10	179.88	0.11	179.94	−177.59
				10.35	−173.46	6.80	−172.39	−176.28
TS(11-*cis*/11_14-*cis*)	1.20	3.33		−0.09	179.96	179.97	178.90	−178.23
11-*cis*	0.21	2.79 (1.69)	2.68 (1.59)	0.52	−179.59	180.00	180.00	−177.54
				−10.75	172.85	175.27	172.29	−174.59
CI(11-*cis*/11_14-*cis*)	3.96	4.09		1.97	−173.95	−175.72	174.95	173.30
11_14-*cis*	0.41	2.89 (1.39)	2.82 (1.35)	10.45	−173.52	−177.03	−171.66	−176.22
				13.74	−170.61	−174.42	−168.58	−178.10
TS(11-*cis*/9_11-*cis*)	1.59	2.23		17.21	−164.28	92.72	−178.23	175.97
CI(11-*cis*/9_11-*cis*)	2.74	2.78		23.55	−164.21	92.75	178.97	175.37
CI(AT/9-*cis*)	2.94	3.10		178.61	0.49	−84.38	−175.70	−173.32
9-*cis*	0.08	2.61 (1.33)	2.53 (1.35)	179.75	−0.08	−0.43	−179.93	177.60
				179.97	0.06	−0.17	179.88	178.10
8-*cis*	0.11	2.65 (1.73)	2.51 (1.73)	179.79	−0.26	−177.69	−179.66	17.21
				−179.87	0.12	−178.92	−179.62	5.41
RS(AT/9-*cis*)	3.13	3.68		179.92	−0.02	−86.62	−179.97	179.76

zones within the lower energy conditions. We first optimized the transition states for every isomer pair, and then we obtained three transition states (TS(all-*trans*/11-*cis*), TS(11-*cis*/11_14-*cis*), and TS(11-*cis*/9_11-*cis*)) and four rotation states (RS(all-*trans*/7_8-*cis*), RS(all-*trans*/8_11-*cis*), RS(all-*trans*/9_11-*cis*), and RS(all-*trans*/9-*cis*)). Then, we carried out frequency calculations for these seven transition states: a transition state that has one imaginary frequency is named TS, while a transition state that has more than one imaginary frequency is named RS. The three transition states and four rotation states are summarized in Table 1, and the corresponding Cartesian coordinates are given in Table S2 (ESI†). The main focus in photoisomerization dynamics is to find conical intersections, so a real transition state (TS) and an approximated transition

state (RS) are just intermediate processes equally good for finding CIs in the present study.

Now, we performed global trajectory surface hopping dynamics simulations, initially starting from each transition and rotation state vertically excited to the S_1 state, and for each TS or RS we ran a few tens of sampling trajectories and determined the hopping zone from which one representative CI can be specified. We finally found seven conical intersections, namely CI(all-*trans*/7_8-*cis*) with $(\alpha, \mu) = (−179.9°, 91.8°)$, CI(all-*trans*/11-*cis*) with $\alpha = −99.2°$, CI(all-*trans*/8_11-*cis*) with $(\alpha, \varepsilon) = (−88.7°, −98.6°)$, CI(all-*trans*/9_11-*cis*) with $(\alpha, \beta) = (−80.3°, 85.6°)$, CI(11-*cis*/11_14-*cis*) with $(\alpha, \theta) = (2°, 104.5°)$, CI(11-*cis*/9_11-*cis*) with $(\alpha, \gamma) = (23.6°, 92.8°)$, and CI(all-*trans*/9-*cis*) with $(\alpha, \gamma) = (178.6°, −84.4°)$, as shown in Table 1, and the corresponding Cartesian coordinates are given in Table S3 (ESI†). The electronic structures of all seven conical intersections are drawn in Fig. S3 (ESI†). We carried out calculations of the natural transition orbitals at each representative conical intersection, as shown in Fig. S4 (ESI†), and we found that the $S_0 \rightarrow S_1$ electronic transition at each CI is dominantly contributed to by HOMO to LUMO transfer. The HOMO and LUMO charge distributions are mostly concentrated at the side-chain chromophore around the α dihedral angle, with charge transfer to the LUMO around the other dihedral angle for each of the six low-layer-energy CI zones (not including CI(all-*trans*/7_8-*cis*) in
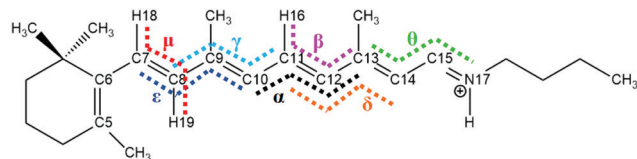

Fig. 1 The numbering of atoms in the backbone of all-*trans* RPSB. Seven specific dihedral angles (arranged from left to right) are important for the conical intersections, namely ε: $C_7C_8C_9C_{10}$; μ: $H_{18}C_7C_8H_{19}$; γ: $C_8C_9C_{10}C_{11}$; α: $C_{10}C_{11}C_{12}C_{13}$; β: $H_{16}C_{11}C_{12}H_{13}$; δ: $C_{11}C_{12}C_{13}C_{14}$; and θ: $C_{13}C_{14}C_{15}N_{17}$.

23864 | *Phys. Chem. Chem. Phys.*, 2021, **23**, 23861–23874

This journal is © the Owner Societies 2021

Table 2 The energies of the S_0 and S_1 states of RPSBT isomers calculated using the present (TD)CAM-B3LYP/6-31G method compared with results calculated *via* the M06-2X/cc-pVDZ method found in the literature. The present calculated adiabatic S_1 state energies are also shown in parentheses

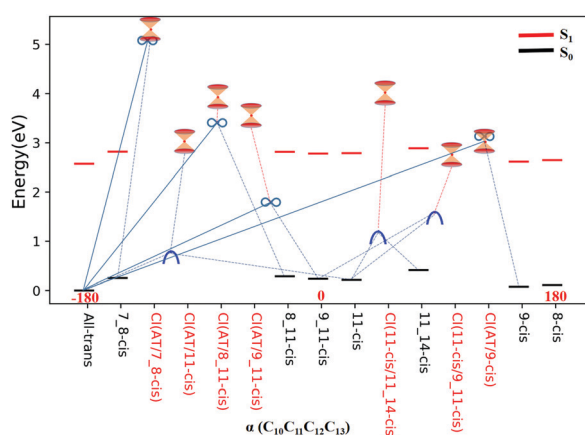| Structure	Potential energy		
	S_0 $(S_1(MIN))$	$S_0{}^a$	$S_0{}^b$
All-*trans*	0.00 (2.48)	0.00	0.00
7_8-*cis*	0.25		0.18
8_11-*cis*	0.28 (2.69)		0.34
9_11-*cis*	0.24 (2.70)		0.28
11-*cis*	0.21 (2.68)	0.21	0.21
11_14-*cis*	0.41 (2.82)		0.43
9-*cis*	0.08 (2.53)	0.06	0.06
8-*cis*	0.11 (2.51)	0.12	0.12

^{a} Ref. 16. ^{b} Ref. 38.

Fig. 2 Potential energy profiles for the RPSB isomers given in Table 1, the seven representative CIs, three TSs, and four RSs, and eight S_0 minima with respect to the α dihedral angle. The vertical excitation energies at the eight S_0 minima are marked with red dashes. The seven double funnels represent CIs. The three blue convex curves represent TSs and the four black ∞ symbols represent RSs. Each TS or RS is linked with the pairwise isomer where it was originally found.

Fig. S4a (ESI†), which is in the high-energy zone). This confirms again that the six low-layer-energy CI zones correspond to photoisomerization dynamics under experimental conditions.

All eight isomers in the ground state, three transition states, four rotation states, and seven conical intersections are summarized in Table 1, ranked from smallest to largest dihedral angle (α = $C_{10}C_{11}C_{12}C_{13}$). Fig. 2 shows the potential energy profiles of all critical structure points in Table 1 arranged from an α dihedral angle of −180° to +180°. We noticed that six of the conical intersections have a crossing energy of around 3–4 eV, belonging to the low-layer-energy region, but the other one, CI(all-*trans*/7_8-*cis*), has an energy of 5.3 eV, belonging to the high-energy region, as the total energy for sampling trajectories is close to 8 eV in this case (this example will not be discussed below since we have already neglected high-layer-energy CIs). All sampling trajectories are performed with a total energy of around 5 eV for the other six CIs.

3. Results and discussion

For realistic trajectory surface hopping molecular dynamics simulations of real RPSB systems, the initial conditions for sampling trajectories have to match TS and RS geometries vertically excited to the S_1 state (not in the Franck–Condon region), and only in this way can the present simulation reach lower-energy conical intersection zones. The choice of the initial conditions for sampling trajectories in the TS or RS can involve problems relating to the initial velocity direction in the dimension associated with the imaginary frequency direction. We developed a scheme to choose the correct ratio between forward and backward velocity directions along the reaction coordinate (the imaginary frequency direction) *via* satisfying the correct quantum flux boundary conditions.[49] However, we do not use this scheme in the present simulation with these six CIs because we know that effects will get smaller and smaller as the number of dimensions in the system gets larger and larger. In fact, we compared the simulated results for sampling trajectories with and without this scheme in ref. 49, and we found no noticeable differences. Simulated quantum yields can still be meaningful as the potential energy surface topology around the CI basically determines the trajectory bifurcation ratios. However, the lifetime of the dynamics is not able to be estimated. Initial velocities of sampling trajectories are randomly generated *via* distributing an initial kinetic energy of 2 eV equally to all degrees of freedom at 300 K in the gas phase.[47] A total of 220 sampling trajectories, initially starting from three RS and three TS, as shown in Fig. 3, are performed with a time step of 0.5 fs up to the time constant of 1000 fs. After hopping to the S_0 state for all sampling trajectories, the products are collected and identified when sampling trajectories involve structures with regular oscillating motion.

3.1. Photo isomerization mechanism and quantum yields

Fig. 3a shows that total 50 sampling trajectories start from TS(all-*trans*/11-*cis*) vertically excited to the S_1 state, and 26 make hops around CI(all-*trans*/11-*cis*) to the S_0 state at two dihedral angles α (−100°) and β (92°); the hopping spots are plotted in Fig. 4a. Finally, 15 trajectories end at the 11-*cis* isomer and 11 end at the all-trans isomer, but 24 trajectories run over a potential energy barrier of 12 kcal mol^{-1} in the S_1 state and are trapped in an all-*trans* S_1 minimum as resonance trajectories. Synchronous twisting clockwise C11-H, anticlockwise C12-H, and C13-CH$_3$ motion can facilitate the generation of the 11-*cis* product, while the all-*trans* product is generated *via* clockwise rotation around C11-H first followed by clockwise rotation around C12-H.

Fig. 3b shows that 30 total sampling trajectories start from RS(all-*trans*/8_11-*cis*) vertically excited to the S_1 state, and all make hops around CI(all-*trans*/8_11-*cis*) to the S_0 state at two dihedral angles ε (−98°) and β (89°); the hopping spots are plotted in Fig. 4b. Finally, 24 trajectories end in the all-*trans* isomer and 6 end in the 8-*cis* isomer (none end at 8_11-*cis*). Anticlockwise rotation around C10-H followed by the synchronous clockwise twisting motion of C7-H and C8-H can facilitate the generation of the 8-*cis* product, while the all-*trans* product is

This journal is © the Owner Societies 2021

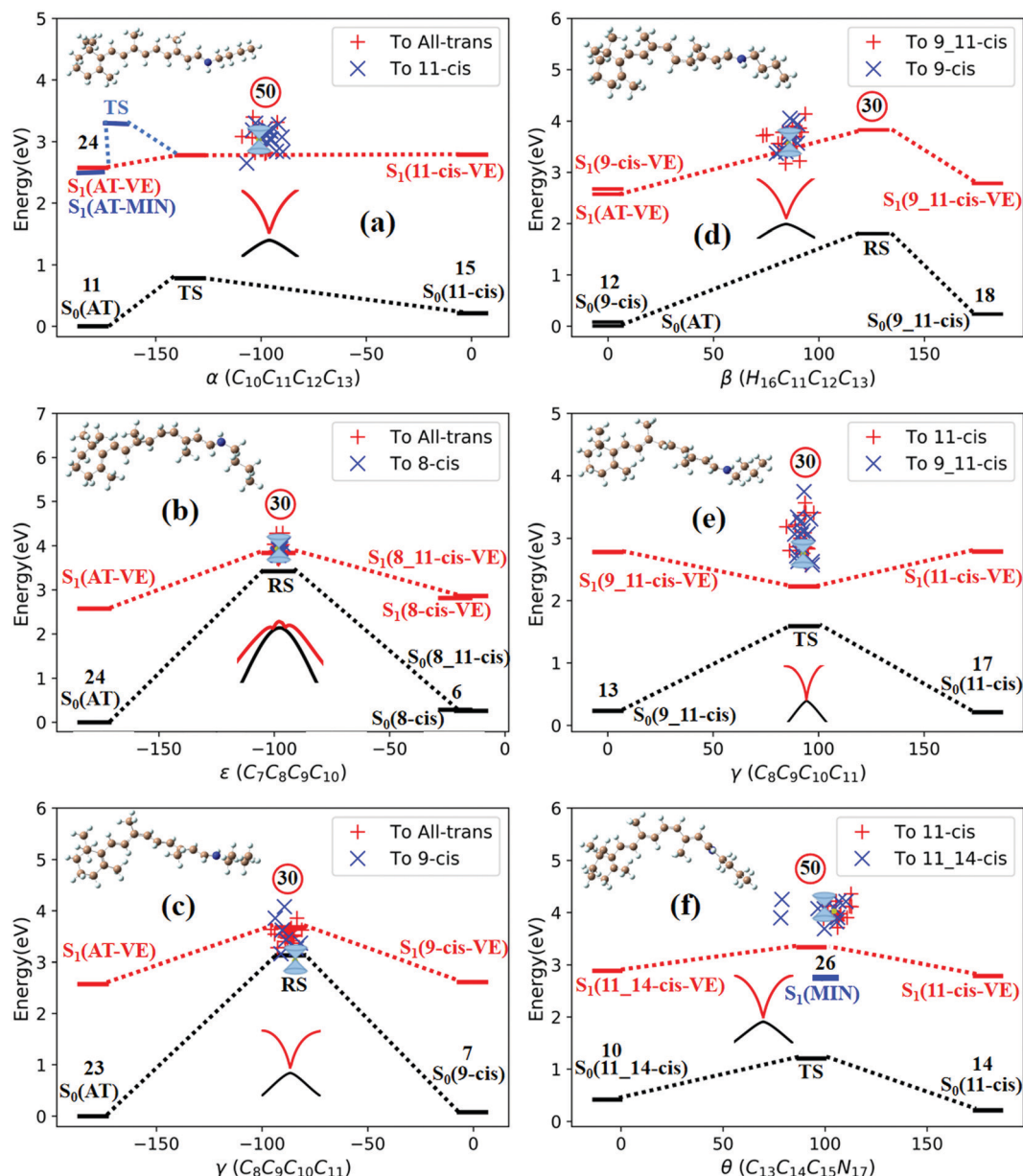*Phys. Chem. Chem. Phys.*, 2021, **23**, 23861–23874 | **23865**

Fig. 3 Potential energy profiles for three TSs and three RSs in the lower-energy zone of CIs with respect to the characteristic dihedral angle; '+' and '×' represent hopping points for sampling trajectories ending in different products. The numbers in the circles represent the number of initial sampling trajectories related to each TS or RS. The double funnels are CIs (the scanned MECI PES around the CI is plotted). (a) TS(all-*trans*/11-*cis*), (b) RS(all-*trans*/8_11-*cis*), (c) RS(all-*trans*/9-*cis*), (d) RS(all-*trans*/9_11-*cis*), (e)TS(11-*cis*/9_11-*cis*), and (f) TS(11-*cis*/11_14-*cis*).

generated by the synchronous anticlockwise twisting motion of C7-H and C8-H.

Fig. 3c shows that a total of 30 sampling trajectories start from RS(all-*trans*/9-*cis*) vertically excited to the S_1 state, and all make hops around CI(all-*trans*/9-*cis*) to the S_0 state at two dihedral angles γ ($-90°$) and β ($0°$); the hopping spots are plotted in Fig. 4c. Finally, 23 trajectories end in the all-*trans* isomer and 7 end in the 9-*cis* isomer. The synchronous twisting clockwise C10-H and anticlockwise C11-H motion can facilitate the generation of both 9-*cis* and all-*trans* products.

Fig. 3d shows that a total of 30 sampling trajectories start from RS(all-*trans*/9_11-*cis*) vertically excited to the S_1 state, and

all make hops around CI(all-*trans*/9_11-*cis*) to the S_0 state at two dihedral angles β ($85°$) and α ($-100°$); the hopping spots are plotted in Fig. 4d. Finally, 12 trajectories end in the 9-*cis* isomer and 18 end in the 9_11-*cis* isomer (none end in all-*trans*). The synchronous anticlockwise twisting motion of C10-H, C11-H, C12-H, and C13-CH$_3$ can facilitate the generation of the 9_11-*cis* product, while the synchronous twisting anticlockwise C10-H and C11-H motion and clockwise C12-H and C13-CH$_3$ motion can facilitate the generation of the 9-*cis* product.

Fig. 3e shows that a total of 30 sampling trajectories start from TS(11-*cis*/9_11-*cis*) vertically excited to the S_1 state, and all make hops around CI(11-*cis*/9_11-*cis*) to the S_0 state at two

23866 | *Phys. Chem. Chem. Phys.*, 2021, **23**, 23861–23874
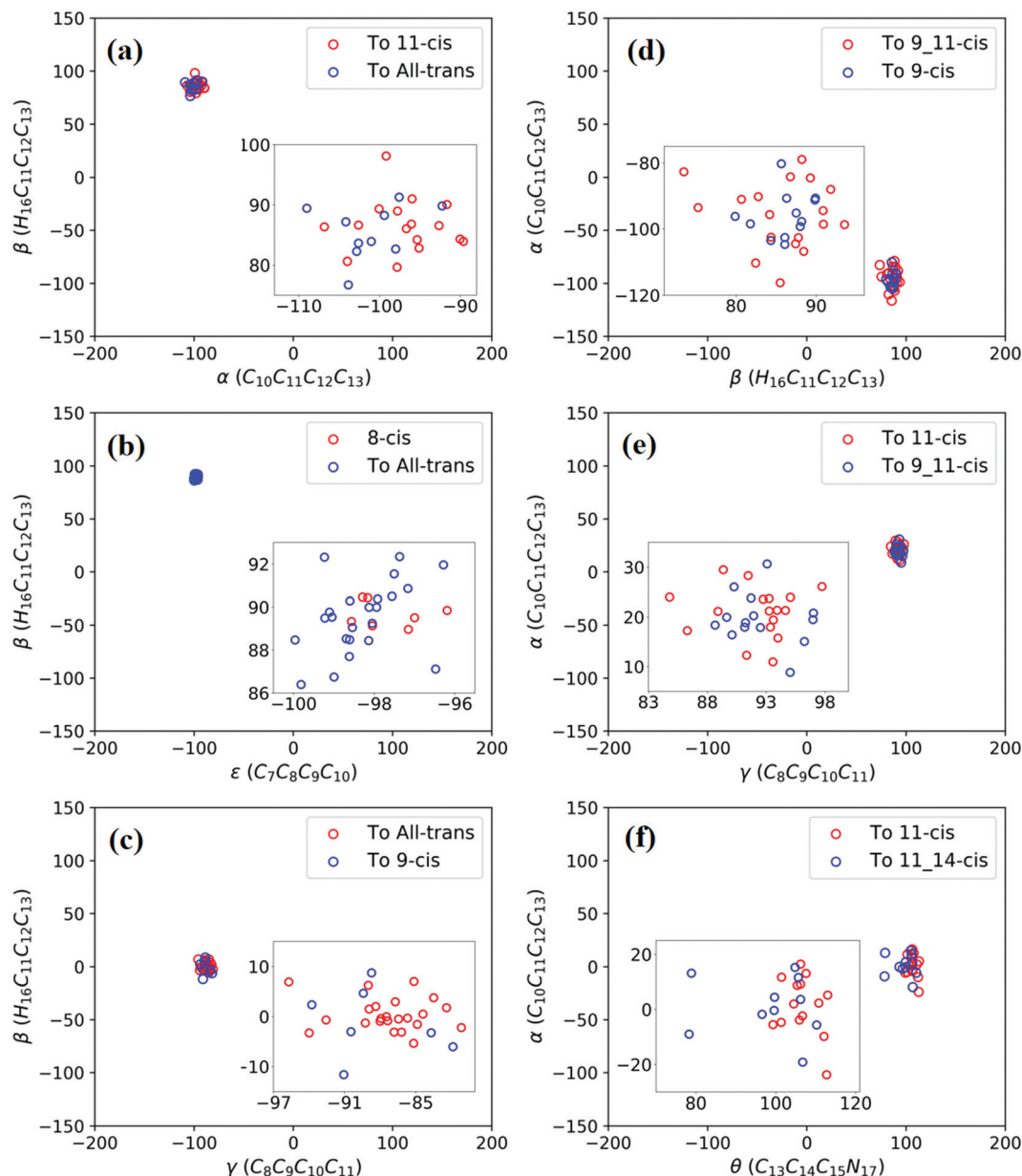
This journal is © the Owner Societies 2021

Fig. 4 Trajectories of hopping-spot distributions with respect to two characteristic dihedral angles for each CI shown in Fig. 3. Enlarged views of the distributions are also plotted. (a) TS(all-*trans*/11-*cis*), (b) RS(all-*trans*/8_11-*cis*), (c) RS(all-*trans*/9-*cis*), (d) RS(all-*trans*/9_11-*cis*), (e) TS(11-*cis*/9_11-*cis*), and (f) TS(11-*cis*/11_14-*cis*).

dihedral angles γ (92°) and α (20°); the hopping spots are plotted in Fig. 4e. Finally, 17 trajectories end in the 11-*cis* isomer and 13 end in the 9_11-*cis* isomer. The synchronous clockwise twisting motion of C10-H, C11-H, C12-H, and C13-CH$_3$ can facilitate the generation of the 9_11-*cis* product, while the synchronous anticlockwise twisting motion of C10-H, C11-H, C12-H, and C13-CH$_3$ can facilitate the generation of the 11-*cis* product.

Fig. 3f shows that a total of 50 sampling trajectories start from TS(11-*cis*/11_14-*cis*) vertically excited to the S$_1$ state, and 24 make hops around CI(11-*cis*/11_14-*cis*) to the S$_0$ state at two dihedral angles θ (110°) and α (0°); the hopping spots are

plotted in Fig. 4d. Finally, 14 trajectories end in the 11-*cis* isomer and 10 end in the 11_14-*cis* isomer, but 26 trajectories are trapped in the S$_1$ minimum at θ = 100° around TS(11-*cis*/11_14-*cis*) as resonance trajectories. The synchronous clockwise twisting motion of C15-H and N17-H can facilitate the generation of the 11_14-*cis* product, while the synchronous anticlockwise twisting motion of C15-H and N17-H can facilitate the generation of the 11-*cis* product.

The quantum yields of RPSB photoisomerization can be estimated from a way in which the sampling trajectories starting from a TS or RS in Fig. 3 can be considered as initial sampling trajectories starting from either side of a TS or RS.

Table 3 Simulated quantum yields (QY) of various isomers from sampling trajectories initially starting from all-*trans* (140) and 11-*cis* (130) isomers. N_{traj} represents the number of trajectories reaching the corresponding isomer

Product	From all-*trans* (140)		From 11-*cis* (130)	
	N_{traj}	QY	N_{traj}	QY
All-*trans*	58	0.41	11	0.08 (0.2[b], 0.65[c])
11-*cis*	15	0.11 (0.09[a])	46	0.35
8-*cis*	6	0.04		
9-*cis*	19	0.14 (0.02)[a]		
9_11-*cis*	18	0.13	13	0.1
11_14-*cis*			10	0.08

[a] Ref. 2. [b] Ref. 11 in methanol solution. [c] Ref. 8 in rhodopsin protein.

Then, we can collect 140 sampling trajectories starting from the all-*trans* region (see Fig. 3a–d) and 130 sampling trajectories starting from the 11-*cis* region (see Fig. 3a, e and f). Therefore, we can estimate a quantum yield of 0.11 from all-*trans* to 11-*cis*, which agrees with the measured value of 0.09 in methanol solution[2] and a yield of 0.08 from 11-*cis* to all-*trans*, which is slightly smaller than the measured value of 0.2 in methanol solution.[11] Simulated quantum yields to various isomer photoproducts are also summarized in Table 3. Potential energy surfaces along MECI at each CI are scanned *via* (TD)-CAM-B3LYP/6-31G with respect to the characteristic dihedral angle for CI(all-*trans*/11-*cis*), CI(all-*trans*/8_11-*cis*), CI(all-*trans*/9-*cis*), CI(all-*trans*/9_11-*cis*), CI(11-*cis*/9_11-*cis*), and CI(11-*cis*/11_14-*cis*). They all show well-behaved potential energy surface topology at conical intersections between the S_1 and S_0 states, as shown in Fig. S5 (ESI†).

3.2. Typical trajectories in terms of five characteristic dihedral angles

A total of 220 sampling trajectories are initially started from three TSs and three RSs, vertically excited to the S_1 state; 170 sampling trajectories hop to the ground S_0 state and 50 sampling trajectories are trapped in potential energy wells in the S_1 state. We discuss how some typical trajectories propagate on the S_0 and S_1 potential energy surfaces in terms of changes to five characteristic dihedral angles (α, β, γ, δ, and ε) and reveal some properties of reactive and nonreactive photoisomerization.

Fig. 5a shows that a typical trajectory starting from TS(all-*trans*/11-*cis*) vertically excited to the S_1 state hops to the S_0 state at 537.5 fs *via* a CI(all-*trans*/11-*cis*)-related event, as shown in Fig. 3a, and it then quickly relaxes to the all-*trans* isomer at 600 fs, as shown in Fig. 5d, where α goes to $-180°$ from $-120°$ and β goes to $0°$ from $50°$ (the other three angles γ, δ, and ε are almost unchanged with only small vibrations). Four double bonds (C7=C8, C9=C10, C11=C12, and C13=C14) vibrate within the range of 0.05 Å, as shown in Fig. S6a (ESI†). Fig. 5b shows that a typical trajectory starting from RS(all-*trans*/8_11-*cis*) vertically excited to the S_1 state hops to the S_0 state at 1.5 fs *via* a CI(all-*trans*/8_11-*cis*)-related event, as shown in Fig. 3b, and it then slowly relaxes to the all-*trans* isomer at 80 fs, as shown in Fig. 5e, where ε and α go to $-180°$ from $-100°$ and β goes to $0°$ from $90°$ (the other two angles γ and δ are almost unchanged).

Two double bonds (C11=C12 and C13=C14) vibrate within a large range of 0.2 Å, as shown in Fig. S6b (ESI†). Fig. 5c shows that a typical trajectory starting from RS(all-*trans*/9-*cis*) vertically excited to the S_1 state hops to the S_0 state at 32 fs *via* a CI(all-*trans*/9-*cis*)-related event, as shown in Fig. 3c, and it then slowly relaxes to the all-*trans* isomer beyond 140 fs, as shown in Fig. 5f, where γ goes to $-180°$ from $-100°$ with slow oscillation (the other four angles α, β, ε, and δ are almost unchanged). The double bond C9=C10 vibrates within the range of 0.3 Å (the other three bonds C7=C8, C11=C12, and C13=C14 vibrate within the range of 0.1 Å), as shown in Fig. S6c (ESI†).

Fig. 6a shows that a typical trajectory starting from TS(all-*trans*/11-*cis*) vertically excited to the S_1 state hops to the S_0 state at 100 fs *via* a CI(all-*trans*/11-*cis*)-related event, as shown in Fig. 3a, and it then relaxes to the 11-*cis* isomer at 300 fs, as shown in Fig. 6d, where α goes to $0°$ from $-140°$ and β goes to $180°$ from $50°$ (the other three angles γ, δ, and ε are almost unchanged with only small vibrations). Four double bonds (C7=C8, C9=C10, C11=C12, and C13=C14) vibrate within the range of 0.05 Å, as shown in Fig. S6d (ESI†). Fig. 6b shows that a typical trajectory starting from RS(all-*trans*/8_11-*cis*) vertically excited to the S_1 state hops to the S_0 state at 1.5 fs *via* a CI(all-*trans*/8_11-*cis*)-related event, as shown in Fig. 3b, and it then slowly relaxes to the 8-*cis* isomer at 180 fs, as shown in Fig. 6e, where ε (β) goes to $0°$ from $-100°$ ($100°$), and α goes to $-180°$ from $-100°$ (the other two angles γ and δ are almost unchanged). The double bond C11=C12 vibrates within the large range of 0.2 Å, as shown in Fig. S6e (ESI†). Fig. 6c shows that a typical trajectory starting from RS(all-*trans*/9-*cis*) vertically excited to the S_1 state hops to the S_0 state at 29.5 fs *via* a CI(all-*trans*/9-*cis*)-related event, as shown in Fig. 3c, and it then relaxes to the 9-*cis* isomer at 120 fs, as shown in Fig. 6f, where γ goes to $0°$ from $-100°$ smoothly (the other four angles α, β, ε, and δ are almost unchanged). The double bond C9=C10 vibrates within the range of 0.3 Å (the other three bonds C7=C8, C11=C12, and C13=C14 vibrate within the range of 0.1 Å), as shown in Fig. S6f (ESI†).

Fig. 7a shows that a typical trajectory starting from RS(all-*trans*/9_11-*cis*) vertically excited to the S_1 state hops to the S_0 state at 44.5 fs *via* a CI(all-*trans*/9_11-*cis*)-related event, as shown in Fig. 3d, and it then relaxes to the 9_11-*cis* isomer at 120 fs, as shown in Fig. 7d, where α and γ go to $0°$ from $-60°$ and β goes to $180°$ from $120°$ (the other two angles δ and ε are almost unchanged with only small vibrations). Two double bonds (C9=C10 and C11=C12) vibrate within the range of 0.25 Å, as shown in Fig. S7a (ESI†). Fig. 7b shows that a typical trajectory starting from TS(11-*cis*/9_11-*cis*) vertically excited to the S_1 state hops to the S_0 state at 10.5 fs *via* a CI(11-*cis*/9_11-*cis*)-related event, as shown in Fig. 3e, and it then relaxes to the 11-*cis* isomer at 70 fs, as shown in Fig. 7e, where γ goes to $180°$ from $90°$ and α goes to $-10°$ from $10°$ (the other three angles β, δ, and ε are almost unchanged with only small vibrations). Two double bonds (C9=C10 and C11=C12) vibrate within the range of 0.15 Å, as shown in Fig. S7b (ESI†). Fig. 7c shows that a typical trajectory starting from TS(11-*cis*/11_14-*cis*) vertically excited to the S_1 state hops to the S_0 state at 881 fs *via* a

23868 | *Phys. Chem. Chem. Phys.*, 2021, **23**, 23861–23874

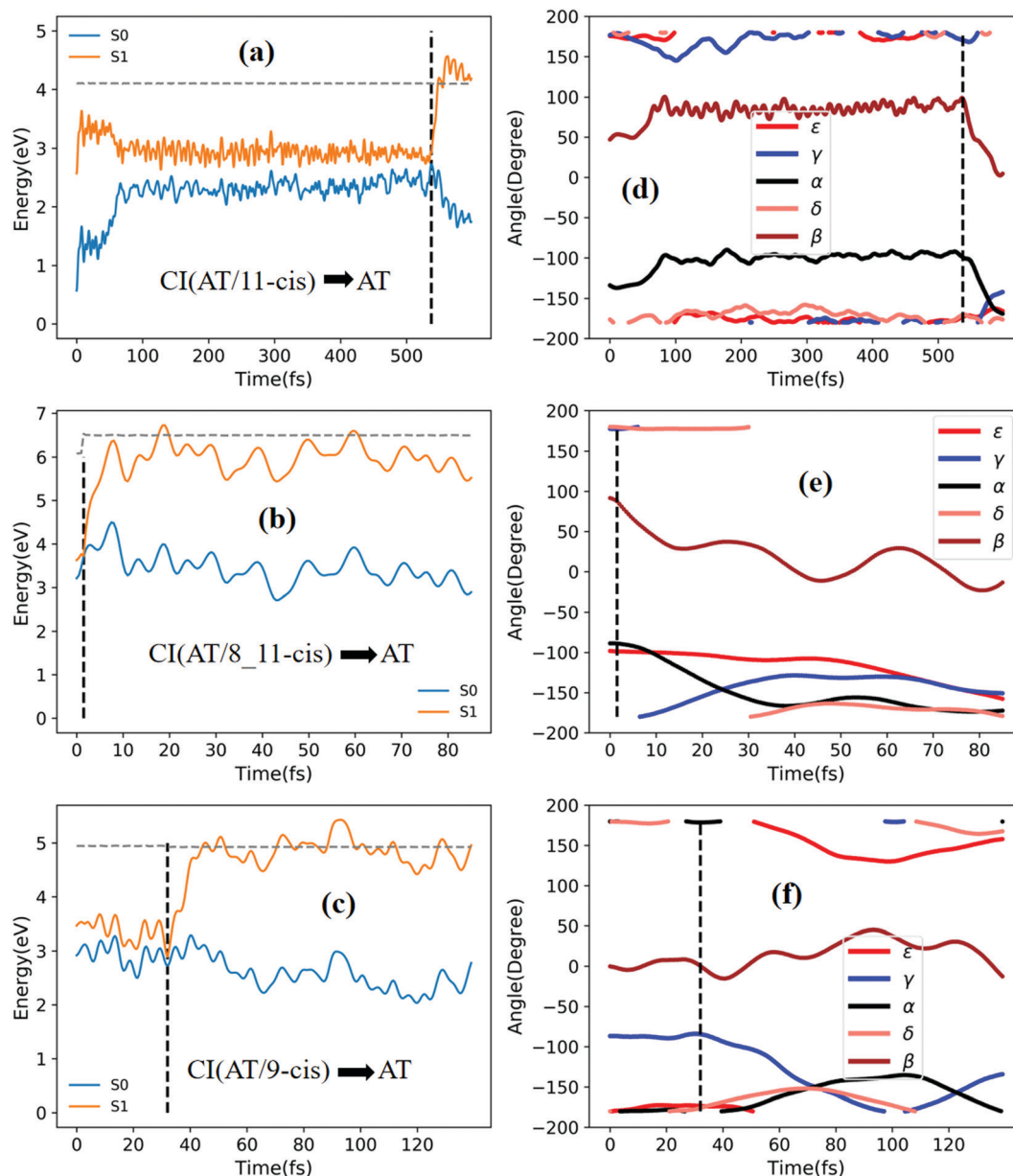This journal is © the Owner Societies 2021

Fig. 5 Potential energy profiles of the S_0 and S_1 states and the corresponding five characteristic dihedral angles as a function of time (the horizontal dashed lines indicate the total energies). Starting from the S_1 state: (a) and (d) going from TS(all-*trans*/11-*cis*) to the all-*trans* product; (b) and (e) going from RS(all-*trans*/8_11-*cis*) to the all-*trans* product; and (c) and (f) going from RS(all-*trans*/9-*cis*) to the all-*trans* product.

CI(11-*cis*/11_14-*cis*)-related event, as shown in Fig. 3f, and it then relaxes to the 11-*cis* isomer at 1000 fs, as shown in Fig. 7f where θ (not given in Table 1), as seen in Fig. 1, goes to 180° from 90° (the five angles α, β, γ, δ, and ε are almost unchanged with only small vibrations). Four double bonds (C7=C8, C9=C10, C11=C12, and C13=C14) vibrate rapidly within the range of 0.10 Å, as shown in Fig. S7c (ESI†).

Fig. 8a shows that a typical trajectory starting from RS(all-*trans*/9_11-*cis*) vertically excited to the S_1 state hops to the S_0 state at 173.5 fs *via* a CI(all-*trans*/9_11-*cis*)-related event, as shown in Fig. 3d, and it then relaxes to the 9-*cis* isomer at 280 fs, as shown in Fig. 8d, where α goes to −180° from −50°,

γ goes to 0° from −60°, and β goes to 120° from 0° (the other two angles δ and ε are almost unchanged with only small vibrations). Two double bonds (C9=C10 and C11=C12) vibrate within the range of 0.20 Å, as shown in Fig. S7d (ESI†). Fig. 8b shows that a typical trajectory starting from TS(11-*cis*/9_11-*cis*) vertically excited to the S_1 state hops to the S_0 state at 8.5 fs *via* a CI(11-*cis*/9_11-*cis*)-related event, as shown in Fig. 3e, and it then relaxes to the 9_11-*cis* isomer at 120 fs, as shown in Fig. 8e, where γ goes to 0° from 100° (the other four angles α, β, δ, and ε are almost unchanged with only small vibrations). Three double bonds (C9=C10, C11=C12, and C13=C14) vibrate within the range of 0.2 Å, as shown in Fig. S7e (ESI†).
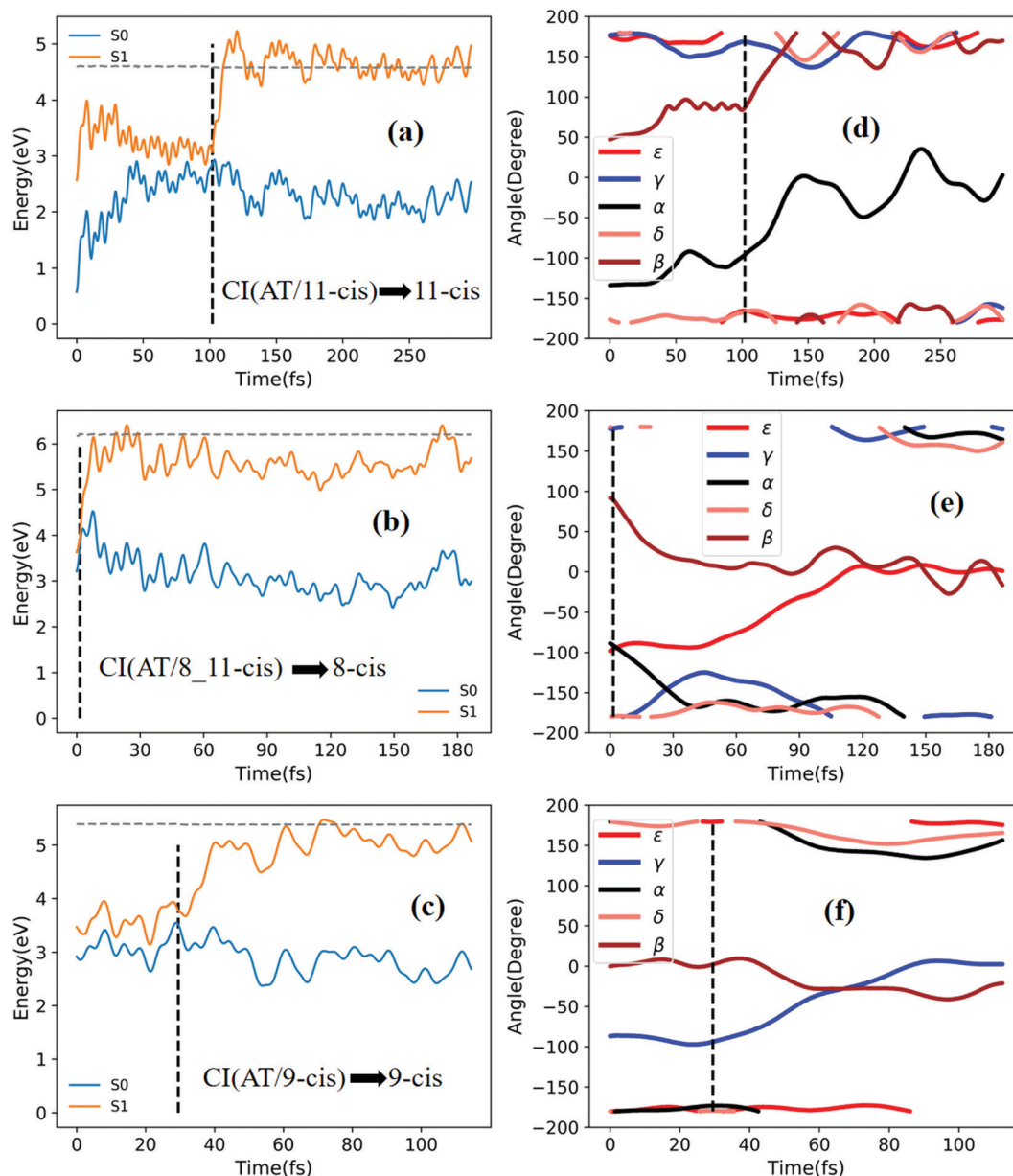
This journal is © the Owner Societies 2021

Phys. Chem. Chem. Phys., 2021, **23**, 23861–23874 | **23869**

Fig. 6 Potential energy profiles of the S_0 and S_1 states and the corresponding five characteristic dihedral angles as a function of time for typical trajectories (the horizontal dashed lines indicate total energies). Starting from the S_1 state: (a) and (d) going from TS(all-*trans*/11-*cis*) to the 11-*cis* product; (b) and (e) going from RS(all-*trans*/8_11-*cis*) to the 8-*cis* product; and (c) and (f) going from RS(all-*trans*/9-*cis*) to the 9-*cis* product.

Fig. 8c shows that a typical trajectory starting from TS(11-*cis*/ 11_14-*cis*) vertically excited to the S_1 state hops to the S_0 state at 852 fs *via* CI(11-*cis*/11_14-*cis*), as shown in Fig. 3f, and it then relaxes to the 11_14-*cis* isomer at 1000 fs, as shown in Fig. 8f, where θ (not given in Table 1), as seen in Fig. 1, goes to 0° from 100° (the five angles α, β, γ, δ, and ε are almost unchanged with only small vibrations). Four double bonds (C7=C8, C9=C10, C11=C12, and C13=C14) vibrate rapidly within the range of 0.10 Å, as shown in Fig. S7f (ESI†).

We have discussed 12 typical sampling trajectories and their dynamic evolution, hopping from the S_1 state to the S_0 state *via* six conical intersections and then bifurcating into the two product regions connected to each CI. The final product

distributions for all sampling trajectories are summarized in Fig. S8 (ESI†), connected to Fig. 3.

4. Concluding remarks

Via performing global switching trajectory surface hopping molecular dynamics simulations using on-the-fly (TD)CAM-B3LYP/6-31G potential energy surfaces for the first-exited S_1 and ground S_0 states, we have simulated real RPSB photo-isomerization dynamics up to S_1 excitation *via* finding the conical intersection networks spanned by six representative CIs. We have found that there are two layers of conical
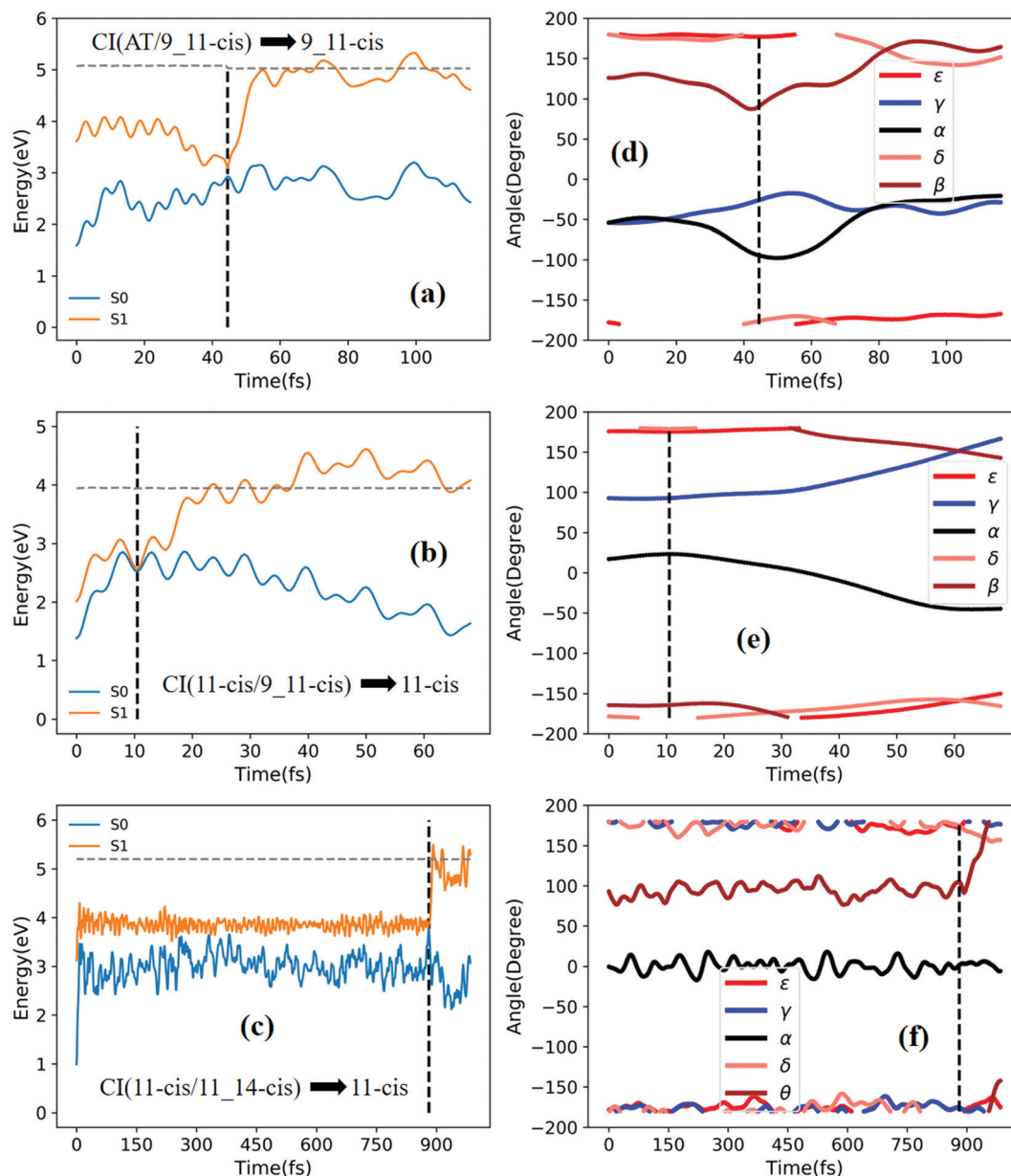
Fig. 7 Potential energy profiles of the S_0 and S_1 states and the corresponding five characteristic dihedral angles as a function of time (the horizontal dashed lines indicate total energies). Starting from the S_1 state: (a) and (d) going from RS(all-*trans*/9_11-*cis*) to the 9_11-*cis* product; (b) and (e) going from TS(11-*cis*/9_11-*cis*) to the 11-*cis* product; and (c) and (f) going from TS(11-*cis*/11_14-*cis*) to the 11-*cis* product.

intersection clouds: one layer has energies as high as 8 eV (above all-*trans* S_0) and the other has low energies of around 3–4 eV. In the present work, we have probed RPSB photoisomerization mechanisms *via* only focusing on low-layer-energy CIs. The present simulation gives a quantum yield of 0.11 (0.08) in the gas phase in comparison to an experimental value of 0.09 (0.2) in solution for all-*trans* to 11-*cis* (11-*cis* to all-*trans*) photoisomerization. The present simulation using (TD)-DFT methods indeed detected potential barriers in both the all-*trans* and 11-*cis* Franck–Condon regions, and the barrier energy in 11-*cis* form is lower than that in all-*trans*-form. In addition, for this real RPSB system with 63 atoms, there are 183 vibrational degrees of freedom, so the total kinetic energy can quickly

dissipate into massive vibrational modes in the Franck–Condon regions; thus, even a small potential barrier can prevent sampling trajectories from crossing over. Instead, we carried out simulations starting from transition states based on each pair of isomers. We found six transition states (although three of them are called rotation states) *via* optimization; in such a way we can determine the lower-layer-energy conical intersections and dynamic simulations using transition states vertically excited to S_1 states can actually be performed. We found that different geometries at the hopping points give rise to the twisting of specific torsional angles accompanied by variations of C=C double bonds; as a result, electronic quenching occurs near a CI where one or two of the related dihedral angles
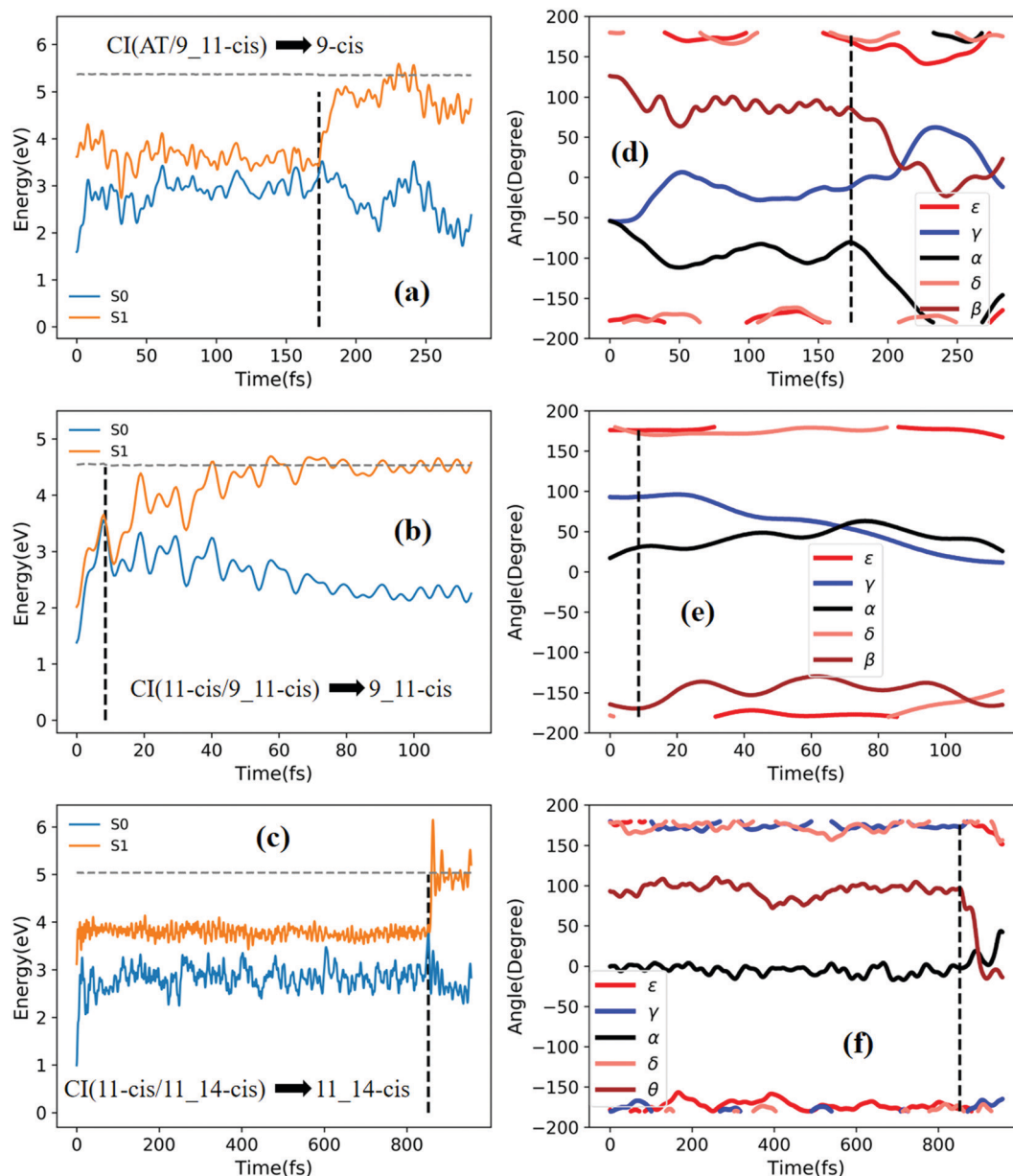
This journal is © the Owner Societies 2021

Phys. Chem. Chem. Phys., 2021, **23**, 23861–23874 | **23871**

Fig. 8 Potential energy profiles of the S_0 and S_1 states and the corresponding five characteristic dihedral angles as a function of time (the horizontal dashed lines indicate total energies). Starting from the S_1 state: (a) and (d) going from RS(all-*trans*/9_11-*cis*) to the 9-*cis* product; (b) and (e) going from TS(11-*cis*/9_11-*cis*) to the 9_11-*cis* product; and (c) and (f) going from TS(11-*cis*/11_14-*cis*) to the 11_14-*cis* product.

related to specific double bonds twist close to 90°. The photo-isomerization reaction is not stereoselective in the gas phase but presents a mixture of isomers compared to the high specificity obtained with proteins.

The present simulation indicated again that the (TD)CAM-B3LYP/6-31G method can show all hopping points with well-behaved potential energy surface topology at conical intersections between S_1 and S_0 states. This can be seen from the scanned potential energy surfaces along MECI with respect to the characteristic dihedral angles for CI(all-*trans*/11-*cis*), CI(all-*trans*/8_11-*cis*), CI(all-*trans*/9-*cis*), CI(all-*trans*/9_11-*cis*), CI(11-*cis*/9_11-*cis*), and C I(11-*cis*/11_14-*cis*). The present simulation method is very encouraging and may allow us to simulate even larger systems

with conventional TD-DFT methods to examine various retinal Schiff-base photoisomerization dynamics in the real world.

Conflicts of interest

The authors declare no competing financial interests.

Acknowledgements

23872 | *Phys. Chem. Chem. Phys.*, 2021, **23**, 23861–23874

This journal is © the Owner Societies 2021

Notes and references

1 R. Mathies, C. Brito Cruz, W. Pollard and C. Shank, *Science*, 1988, **240**, 777–779.

2 K. A. Freedman and R. S. Becker, *J. Am. Chem. Soc.*, 1986, **108**, 1245–1251.

3 S. L. Logunov and M. A. El-Sayed, *J. Phys. Chem. B*, 1997, **101**, 6629–6633.

4 S. L. Logunov, L. Song and M. A. El-Sayed, *J. Phys. Chem.*, 1996, **100**, 18586–18591.

5 H. Kandori and H. Sasabe, *Chem. Phys. Lett.*, 1993, **216**, 126–172.

6 M. Garavelli, F. Negri and M. Olivucci, *J. Am. Chem. Soc.*, 1999, **121**, 1023–1029.

7 C. Punwong, J. Owens and T. J. Martínez, *J. Phys. Chem. B*, 2015, **119**, 704–714.

8 R. Schoenlein, L. Peteanu, R. Mathies and C. Shank, *Science*, 1991, **254**, 412–415.

9 L. Peteanu, R. Schoenlein, Q. Wang, R. Mathies and C. Shank, *Proc. Natl. Acad. Sci. U. S. A.*, 1993, **90**, 11762–11766.

10 D. Polli, P. Altoè, O. Weingart, K. M. Spillane, C. Manzoni, D. Brida, G. Tomasello, G. Orlandi, P. Kukura, R. A. Mathies, M. Garavelli and G. Cerullo, *Nature*, 2010, **467**, 440–443.

11 R. S. Becker and K. Freedman, *J. Am. Chem. Soc.*, 1985, **107**, 1477–1485.

12 H. Kandori, Y. Katsuta, M. Ito and H. Sasabe, *J. Am. Chem. Soc.*, 1995, **117**, 2669–2670.

13 G. Bassolino, T. Sovdat, A. Soares Duarte, J. M. Lim, C. Schnedermann, M. Liebel, B. Odell, T. D. W. Claridge, S. P. Fletcher and P. Kukura, *J. Am. Chem. Soc.*, 2015, **137**, 12434–12437.

14 G. Zgrablić, A. M. Novello and F. Parmigiani, *J. Am. Chem. Soc.*, 2012, **134**, 955–961.

15 J. Rajput, D. Rahbek, L. Andersen, A. Hirshfeld, M. Sheves, P. Altoè, G. Orlandi and M. Garavelli, *Angew. Chem., Int. Ed.*, 2010, **49**, 1790–1793.

16 N. J. A. Coughlan, K. J. Catani, B. D. Adamson, U. Wille and E. J. Bieske, *J. Chem. Phys.*, 2014, **140**, 164307.

17 H. V. Kiefer, E. Gruber, J. Langeland, P. A. Kusochek, A. V. Bochenkova and L. H. Andersen, *Nat. Commun.*, 2019, **10**, 1210.

18 M. Sun, Y. Ding, G. Cui and Y. Liu, *J. Phys. Chem. A*, 2007, **111**, 2946–2950.

19 P. Zhou, J. Liu, K. Han and G. He, *J. Comput. Chem.*, 2014, **35**, 109–120.

20 A. Cembran, R. González-Luque, P. Altoè, M. Merchán, F. Bernardi, M. Olivucci and M. Garavelli, *J. Phys. Chem. A*, 2005, **109**, 6597–6605.

21 A. Cembran, R. González-Luque, L. Serrano-Andrés, M. Merchán and M. Garavelli, *Theor. Chem. Acc.*, 2007, **118**, 173–183.

22 R. Barata-Morgado, M. L. Sánchez, A. Muñoz-Losa, M. E. Martín, F. J. Olivares del Valle and M. A. Aguilar, *J. Phys. Chem. A*, 2018, **122**, 3096–3106.

23 J. W. Park and T. Shiozaki, *Mol. Phys.*, 2018, **116**, 2583–2590.

24 T. Ishida, S. Nanbu and H. Nakamura, *J. Phys. Chem. A*, 2009, **113**, 4356–4366.

25 O. Weingart, *J. Am. Chem. Soc.*, 2007, **129**, 10618–10619.

26 W. C. Chung, S. Nanbu and T. Ishida, *J. Phys. Chem. A*, 2010, **114**, 8190–8201.

27 T. Vreven, F. Bernardi, M. Garavelli, M. Olivucci, M. A. Robb and H. B. Schlegel, *J. Am. Chem. Soc.*, 1997, **119**, 12687–12688.

28 O. Weingart, I. Schapiro and V. Buss, *J. Phys. Chem. B*, 2007, **111**, 3782–3788.

29 M. Barbatti, G. Granucci, M. Persico, M. Ruckenbauer, M. Vazdar, M. Eckert-Maksić and H. Lischka, *J. Photochem. Photobiol., A*, 2007, **190**, 228–240.

30 M. Barbatti, M. Ruckenbauer, J. J. Szymczak, A. J. A. Aquino and H. Lischka, *Phys. Chem. Chem. Phys.*, 2008, **10**, 482–494.

31 O. Weingart, I. Schapiro and V. Buss, *J. Mol. Model.*, 2006, **12**, 713–721.

32 Y. Hu, C. Xu, L. Ye, F. L. Gu and C. Zhu, *Phys. Chem. Chem. Phys.*, 2021, **23**, 5236–5243.

33 L. Yu, C. Xu, Y. Lei, C. Zhu and Z. Wen, *Phys. Chem. Chem. Phys.*, 2014, **16**, 25883–25895.

34 C. Zhu and H. Nakamura, *J. Chem. Phys.*, 1992, **97**, 8497.

35 C. Zhu and H. Nakamura, *J. Chem. Phys.*, 1993, **98**, 6208.

36 M. J. Frisch, G. W. Trucks, H. B. Schlegel, G. E. Scuseria, M. A. Robb, J. R. Cheeseman, G. Scalmani, V. Barone, G. A. Petersson, H. Nakatsuji, X. Li, M. Caricato, A. V. Marenich, J. Bloino, B. G. Janesko, R. Gomperts, B. Mennucci, H. P. Hratchian, J. V. Ortiz, A. F. Izmaylov, J. L. Sonnenberg, D. Williams-Young, F. Ding, F. Lipparini, F. Egidi, J. Goings, B. Peng, A. Petrone, T. Henderson, D. Ranasinghe, V. G. Zakrzewski, J. Gao, N. Rega, G. Zheng, W. Liang, M. Hada, M. Ehara, K. Toyota, R. Fukuda, J. Hasegawa, M. Ishida, T. Nakajima, Y. Honda, O. Kitao, H. Nakai, T. Vreven, K. Throssell, J. A. Montgomery, Jr., J. E. Peralta, F. Ogliaro, M. J. Bearpark, J. J. Heyd, E. N. Brothers, K. N. Kudin, V. N. Staroverov, T. A. Keith, R. Kobayashi, J. Normand, K. Raghavachari, A. P. Rendell, J. C. Burant, S. S. Iyengar, J. Tomasi, M. Cossi, J. M. Millam, M. Klene, C. Adamo, R. Cammi, J. W. Ochterski, R. L. Martin, K. Morokuma, O. Farkas, J. B. Foresman and D. J. Fox, *Gaussian16 (Revision B.01)*, Inc., Wallingford CT, 2016.

37 Z. Cai, M. J. Crossley, J. R. Reimers, R. Kobayashi and R. D. Amos, *J. Phys. Chem. B*, 2006, **110**, 15624–15632.

38 N. J. A. Coughlan, B. D. Adamson, L. Gamon, K. Catani and E. J. Bieske, *Phys. Chem. Chem. Phys.*, 2015, **17**, 22623–22631.

39 P. Hamm, M. Zurek, T. Röschinger, H. Patzelt, D. Oesterhelt and W. Zinth, *Chem. Phys. Lett.*, 1996, **263**, 613–621.

40 G. Wald and P. K. Brown, *Science*, 1958, **127**, 222–249.

41 J. K. Lanyi, *Nature*, 1995, **375**, 461–463.

42 R. Send, D. Sundholm, M. P. Johansson and F. Paw lowski, *J. Chem. Theory Comput.*, 2009, **5**, 2401–2414.

43 O. Valsson and C. Filippi, *J. Chem. Theory Comput.*, 2010, **6**, 1275–1292.

44 R. Send and D. Sundholm, *J. Phys. Chem. A*, 2007, **111**, 27–33.

45 R. Send and D. Sundholm, *J. Phys. Chem. A*, 2007, **111**, 8766–8773.

46 R. Send and D. Sundholm, *J. Mol. Model.*, 2008, **14**, 717–726.

47 B. Sellner, M. Barbatti and H. Lischka, *J. Chem. Phys.*, 2009, **131**, 024312.

48 O. Weingart, A. Migani, M. Olivucci, M. A. Robb, V. Buss and P. Hunt, *J. Phys. Chem. A*, 2004, **108**, 4685–4693.

49 L. Yue, L. Yu, C. Xu, C. Zhu and Y. Liu, *Phys. Chem. Chem. Phys.*, 2020, **22**, 11440–11451.